International Journal of Mechanical, Industrial and Aerospace Sciences
ISSN: 2517-9950
Vol:7, No:6, 2013

Concentrated Solar Power Utilization in Space Vehicles Propulsion and Power Generation

Maged A. Mossallam

***Abstract*—**The objective from this paper is to design a solar thermal engine for space vehicles orbital control and electricity generation. A computational model is developed for the prediction of the solar thermal engine performance for different design parameters and conditions in order to enhance the engine efficiency. The engine is divided into two main subsystems. First, the concentrator dish which receives solar energy from the sun and reflects them to the cavity receiver. The second one is the cavity receiver which receives the heat flux reflected from the concentrator and transfers heat to the fluid passing over. Other subsystems depend on the application required from the engine. For thrust application, a nozzle is introduced to the system for the fluid to expand and produce thrust. Hydrogen is preferred as a working fluid in the thruster application. Results model developed is used to determine the thrust for a concentrator dish 4 meters in diameter (provides 10 kW of energy), focusing solar energy to a 10 cm aperture diameter cavity receiver. The cavity receiver outer length is 50 cm and the internal cavity is 47 cm in length. The suggested design material of the internal cavity is tungsten to withstand high temperature. The thermal model and analysis shows that the hydrogen temperature at the plenum reaches 2000^{o}K after about 250 seconds for hot start operation for a flow rate of 0.1 g/sec.Using solar thermal engine as an electricity generation device on earth is also discussed. In this case a compressor and turbine are used to convert the heat gained by the working fluid (air) into mechanical power. This mechanical power can be converted into electrical power by using a generator.

***Keywords*—**Concentrated Solar Energy, Orbital Control, Power Generation, Solar Thermal Engine, Space Vehicles Propulsion.

I. Introduction

CONCENTRATED SOLAR POWER (CSP) showed enormous promise during the second half of the 20th Century. More countries all over the world extended their dependency on CSP technologies either for space or commercial applications on earth for purposes of electricity generation and solar heating. The amount of usable power achieved from CSP systems is significant compared with non concentrating devices which enables its usage in more advanced applications such as space thrust and electrical power generation discussed in the present paper. The idea of solar thermal concentration is simply to collect solar rays using concentrator and to focus them on a receiver to heat the working fluid.

In this paper solar energy conversion is considered for two applications. One application is related to space thrust as shown in Fig. 1. In another application, solar energy will be used to produce electric energy. For thrust and electricity generation the basic solar collection subsystems (concentrator and receiver) remain the same.

M. A. Mossallam, National Authority for Remote Sensing and Space Sciences (NARSS), Cairo, Egypt, (e-mail: maged3asem@rocketmail.com).

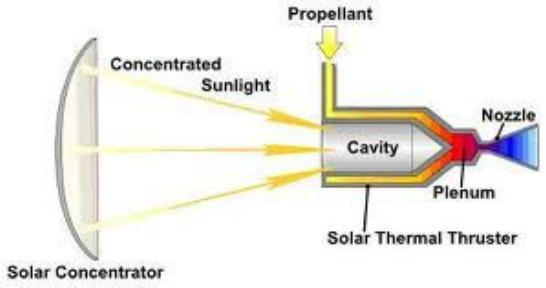

Fig. 1 Solar thermal thruster components

The nozzle is replaced with a compressor turbine assembly connected with a generator for electricity generation as shown in Fig. 2.

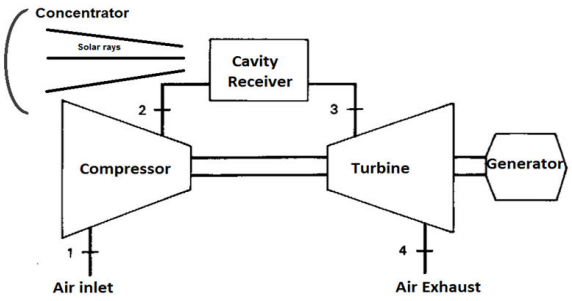

Fig. 2 Schematic of solar thermal power generation cycle

II. Methodology

Concentrator dish analysis is performed using a ray tracing method. A computer code is written to compute the power intercepted by the receiver from the concentrator dish and the effect of changing the dish design parameters on the intercepted power and the optical efficiency. The intercepted power is received by a cavity receiver. The cavity receiver is modeled using an unsteady lumped capacity resistance model. The system is discretized using the finite volume approach. A parametric study is done to the cavity receiver model in a manner to increase the working fluid temperature at plenum. After design and enhancement of the main components of the solar thermal engine (Concentrator and cavity receiver),

matching a nozzle for the propulsion application is considered. The nozzle analysis is done using a quasi-one dimensional model. In the electricity generation application a compressor and turbine are matched with the main components. The thermal cycle of the working fluid is the Brayton cycle that uses the concentrator dish as the source of heat energy.

III. Concentrator Dish Analysis

The main target from the concentrator dish analysis is to determine the amount of energy intercepted by the receiver which will be converted into a usable energy [4]. The total input power intercepted by the receiver is given by,

$$P_{\text{int}} = \rho\tau\alpha I_b \cos\theta_i A_a E_{sh}\phi. \quad (1)$$

Equation (1) shows that the amount of solar radiation reaching the receiver depends on the following parameters. The beam normal insolation incident on the concentrator I_b. Incidence angle of sun rays θ_i which is the angle between sun rays and a line perpendicular to the concentrator aperture plane. Incidence angle equals to zero for the concentrator dish. E_{sh} is the fraction of concentrator aperture area not shaded by the receiver. Radiative material properties for both concentrator and receiver are important factors in raising the system performance [8]. Selection of material with high reflectivity ρ for the concentrator design and other material with high absorptivity α for the receiver increases the intercepted power by the receiver. The term τ represents the transmittance of the glass cover.

The intercept factor ϕ is the fraction of solar radiation reflected from the parabolic concentrator to the receiver aperture which is given by [9],

$$\phi = \frac{P_{\text{int}}}{P_{ref}} = \frac{\sum_0^{\psi_{rim}} \Delta P}{I_b A_p} \quad (2)$$

where I_b is the beam normal insolation from sun rays and A_p is the projected area of the concentrator aperture [10].

The power output from each differential ring ΔP *is* given by,

$$\Delta P = \rho\alpha\Gamma dI_\psi \Delta\psi \quad (3)$$

where ΔP is the power intercepted from a specific ring at angle ψ from the parabolic dish axis, ρ is the mirror specular reflectance, α is the receiver absorptance, Γ is the flux capture fraction for each differential ring, dI_ψ is the change in the radiant flux with respect to the change in the specific ring location on the parabolic dish, and $\Delta\psi$ is the width of the ring in radians. The value of dI_ψ is given by,

$$dI_\psi = \frac{8\pi I_b f^2 \sin\psi}{(1+\cos\psi)^2} \quad (4)$$

The problem of the determination of the flux capture fraction Γ was solved statistically by Stine and Harrigan assuming that the flux is normally distributed and equals to the area under the normal distribution curve [9].

The optical efficiency is given by,

$$\eta_{opt} = E_{sh}(\cos\theta_i)\rho\phi \quad (5)$$

The concentrator dish optical efficiency represents how much solar insolation arriving at the concentrator aperture reflected and passes through the receiver aperture located at the focus [4], [11].

IV. Cavity Receiver Analysis

Conservation of energy principles are applied to discretize the cavity receiver into sub volumes. Each control volume represents a hollow cylinder with four layers in the radial direction. The first layer represents the cavity surface, the second one represents the fluid path, the third one represents the outer cylinder surface and the last layer represents the insulation. The control volume shape changes at the last two sections at the cavity exit. This is to simulate the receiver end and the plenum section of the nozzle or the turbine inlet. A numerical formulation in terms of thermal resistance concept is used for writing the heat transfer equations between each node and its neighbors. Each nodal equation is written in terms of the thermal resistances and thermal capacity of the material. This thermal network between nodes leads to formulation of a transient two dimensional thermal capacity resistance model in cylindrical coordinates (radial and axial). Further illustration for model is shown in Fig. 3.

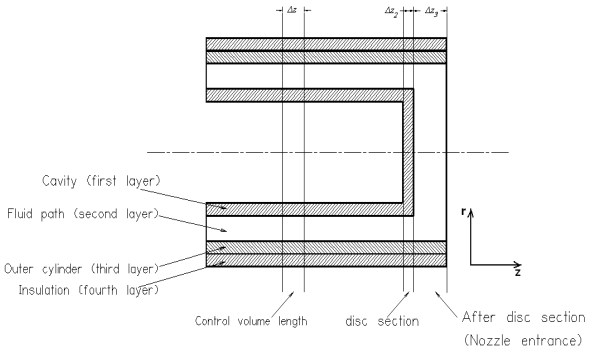

Fig. 3 Cavity receiver discretized layers and sections

The receiver model is discretized in both radial and longitudinal directions into a set of control volumes. Four layers in the radial direction *r* as shown in Fig. 3, each layer is divided axially into sections of length Δz. The control volume length remains uniform until the disc section is reached and then it changes to Δz_2, which is the disc thickness. At the nozzle entrance the control volume length will be Δz_3.

A. Governing Equations

In thermal resistance and capacity formulation, each volume element can be treated as a node which is connected by thermal resistances to its adjoining neighbors. For steady state conditions the net energy transfer into the node equals zero, while for unsteady problems the net energy transfer into the node equals to the increase in the internal energy of the volume [5], [12]. The general energy balance equation on a node using capacity resistance formulation for node *i* is given by,

$$Q_i + \sum_{i,j} \frac{T_{j,i}^{n} - T_{i,j}^{n}}{R_{ij}} = C_i \frac{T_{i,j}^{n+1} - T_{i,j}^{n}}{\Delta \tau} \tag{6}$$

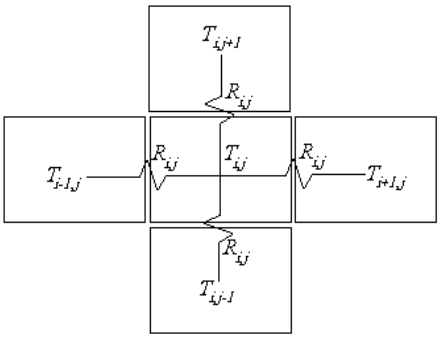

Fig. 4 Temperature nodes and thermal resistances

where Q_i is the heat transferred to node *i*, T_i is the temperature at node *i*, T_j is temperature at neighbor node *j*. R_{ij} is the thermal resistance between node i and neighboring node *j*, depending on heat transfer mode between two nodes either by convection, conduction or radiation, C_i is thermal capacity term, n is the number of time step and $\Delta\tau$ is the time difference between two successive time steps.

Thermal capacity term can be defined as,

$$C_i = \rho_i c_{p_i} \Delta V_i \tag{7}$$

where ρ_i is the material or fluid density at node *i*, ΔV_i is the volume and c_{pi} is the heat capacity of the cavity receiver layer.

The thermal resistance between two neighboring nodes depends on the heat transfer mode between them. In case of conduction heat transfer through a cylinder between 2 nodes the thermal resistance due to conduction is given by [12],

$$R_{cond} = \ln(r_o / r_i) / (2\pi k \Delta z)_i \tag{8}$$

where r_o is the outer radius, r_i is the inner radius, k is the material conductivity and Δz is the control volume length. In case of convection heat transfer the convection thermal resistance is given by,

$$R_{conv} = 1/(h_o A_o) \tag{9}$$

where h_o represents the convection heat transfer coefficient and A_o is the outer surface area of a convective surface. Modeling of convection heat transfer coefficient will be discussed later in the fluid model. In case of radiation heat transfer the radiation thermal resistance is given by,

$$R_{rad} = 1/(\sigma F_{12} A_{rad} \varepsilon) \tag{10}$$

where σ is Boltzmann constant, Arad is the radiation surface area, ε is the emissivity and F_{12} is the view factor between two surfaces of radiation. The view factor will be applied to the internal cavity surface model which will be discussed later in the radiation analysis.

B. Thermal Resistance Network

Each control volume is represented by a single node which is modeled as a lumped capacity.

Fig. 5 shows the network resistance model and the resistances represent the following:

- R_1, R_2 outer radiation resistance between receiver surface and ambient temperature.
- R_3 cavity conduction resistance in axial direction.
- R_4 cavity conduction resistance in radial direction.
- R_5 cavity convection resistance in radial direction.
- R_6 cylinder convection resistance in radial direction.
- R_7 cylinder conduction resistance in axial direction.
- R_8 cylinder conduction resistance in radial direction.
- R_9 insulation conduction resistance in radial direction.
- R_{10} insulation conduction resistance in axial direction.
- R_{d1} disc conduction resistance in radial direction.
- R_{d2} disc conduction resistance in axial direction.
- R_{d3} disc convection resistance in axial direction.

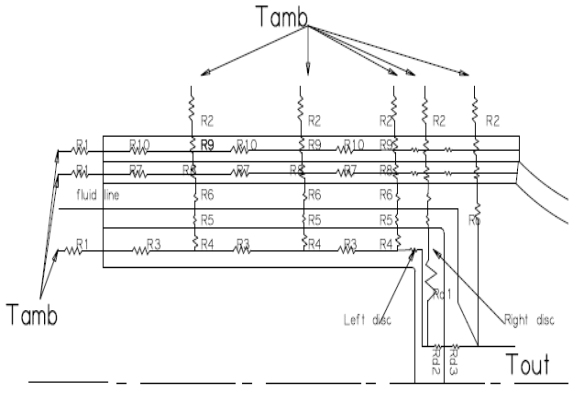

Fig. 5 Thermal resistances network

C. Stability Analysis

The requirement from the stability analysis is to select the optimum time increment $\Delta\tau$ for solving the problem. Equation 5 is solved using forward difference. The resulting equation is an explicit relation to solve for $T_{i,j}^{n+1}$.

$$T_{i,j}^{n+1} = T_{i,j}^{n}\left[1 - \frac{\Delta\tau}{C_i}\sum_{i,j}\frac{1}{R_{ij}}\right] + \frac{\Delta\tau}{C_i}\left[Q_i + \sum_{i,j}\frac{T_{j,i}^{n}}{R_{ij}}\right] \quad (11)$$

For stability, coefficient of $T_{i,j}^{n}$ must be greater than zero, then the stability condition reduces to [12],

$$\Delta\tau \le \frac{C_i}{\sum_{i,j}\frac{1}{R_{ij}}} \quad (12)$$

To ensure the stability $\Delta\tau$ must be kept less than the value of the right hand side for the most restrictive node. Since the problem is solved for large intervals of time therefore it is not efficient to solve with this extremely small time increment. An implicit formulation resolves this issue and the energy equation reduces to,

$$Q_i + \sum_{i,j}\frac{T_{j,i}^{n+1} - T_{i,j}^{n+1}}{R_{ij}} = C_i\frac{T_{i,j}^{n+1} - T_{i,j}^{n}}{\Delta\tau} \quad (13)$$

Applying this equation for every node produces an implicit set of equations that must be solved simultaneously for $T_{i,j}^{n+1}$.

D. Mathematical Model

The mathematical model for the cavity surface is done by applying the heat equation on the cavity surface that receives radiation from the inner side and transfers heat to the fluid. The solar radiation flux intercepted by the cavity receiver Q_{int} was computed from the concentrator dish analysis. Incident radiation flux is assumed to be equally distributed on all sections of cavity walls from the inside. The energy equation applied to each control volume at the inner cavity surface is given by,

$$\rho_{cav}c_{p\,cav}\Delta V_{cav}\frac{T_i^{n+1} - T_i^{n}}{\Delta\tau} = Q_{\text{int}}(2\pi r_1\Delta z) + \frac{T_{i-1,j}^{n} - T_{i,j}^{n}}{R_{cond\_cav\_z}} + \frac{T_{i+1,j}^{n} - T_{i,j}^{n}}{R_{cond\_cav\_z}} + \frac{T_{i,j+1}^{n} - T_{i,j}^{n}}{R_{cond\_cav\_r} + R_{conv\_cav\_r}} \quad (14)$$

The conduction resistance of the cavity in the radial direction is given by,

$$R_{cond\_cav\_r} = \ln(r_2/r_1)/(2\pi k_{cav}\Delta z) \quad (15)$$

where, r_1 and r_2 are the cavity inner and outer radii, respectively. The cavity material conductivity is k_{cav} and Δz is the control volume length. The cavity conduction resistance in the axial direction is calculated from,

$$R_{cond\_cav\_z} = \Delta z/(\pi(r_2^2 - r_1^2)k_{cav}) \quad (16)$$

The cavity convective resistance to the fluid in the radial direction is given by,

$$R_{conv\_cav\_r} = 1/(h_o(2\pi r_2\Delta z)) \quad (17)$$

where h_o is the convection coefficient from the cavity to the fluid. The volume of the cavity is given by,

$$\Delta V_{cav} = \pi(r_2^2 - r_1^2)\Delta z \quad (18)$$

On modeling the heat transfer in the fluid stream, convection effects must be coupled to the heat balance equation for each control volume. To model this process, accurate values for the convection heat transfer coefficient must be obtained. Heat transfer by diffusion is neglected compared to heat transfer by convection in the fluid model [5].

The value of convection heat transfer coefficient can be obtained by,

$$h_c = \frac{k_{fl}N_u}{D} \quad (19)$$

where, D is the diameter of the convective surface. Since the fluid passes in the internal diameter between cavity and outer cylinder then the value of D can be expressed in terms of cavity outer radius (r_2) and cylinder inner radius (r_3).

The Reynolds number depends on the fluid properties and velocity.

$$\text{Re} = \frac{\rho_{fl}u_{fl}D}{\mu} \quad (20)$$

To model the Nusselt number, three empirical relations are used depending on the Reynolds number. If the flow is laminar (Re<2300), the Nusselt number value can be expressed by,

$$Nu = 1.61\left(\text{Re}\,\text{Pr}\left(\frac{D}{L}\right)\right)^{1/3} \quad (21)$$

If the flow is transitional (2300<Re<10000),

$$Nu = 0.116(\text{Re}^{2/3} - 125)\,\text{Pr}^{1/3}\left[1 + \left(\frac{D}{L}\right)^{2/3}\right] \quad (22)$$

In turbulent flow (Re>10000),

$$Nu = 0.023\,\text{Re}^{0.8}\,\text{Pr}^{0.4} \quad (23)$$

At the nozzle plenum section the convection coefficient depends on the disc not the inner cavity surface. The value of D used in Reynolds number identification in this case will change to be equal the outer diameter of the disc. Nusselt

number in laminar and turbulent zones can be determined using the following equations,

In laminar flow,

$$Nu = 0.664\ \mathrm{Re}^{1/2}\ \mathrm{Pr}^{1/3} \tag{24}$$

In turbulent flow,

$$Nu = (0.037\ \mathrm{Re}^{4/5} - 871)\,\mathrm{Pr}^{1/3} \tag{25}$$

Heat balance equation for the fluid stream layer can be written as,

$$\rho_{fl} c_{p\,fl} \Delta V_{fl} \frac{T_i^{n+1} - T_i^n}{\Delta\tau} = \frac{T_{i,j-1}^n - T_{i,j}^n}{R_{cond\_cav\_r} + R_{conv\_cav\_r}} + \frac{T_{i,j+1}^n - T_{i,j}^n}{R_{cond\_cyl\_r} + R_{conv\_cyl\_r}} + \dot{m} c_{p\,fl} (T_{i-1,j}^n - T_{i,j}^n) + \dot{m} c_{p\,fl} (T_{i+1,j}^n - T_{i,j}^n) \tag{26}$$

where, $\dot{m}$ represents the working fluid mass flow rate. Heat equation applied to the surface of the outer cylinder is given by,

$$\rho_{cyl} c_{p\,cyl} \Delta V_{cyl} \frac{T_i^{n+1} - T_i^n}{\Delta\tau} = \frac{T_{i,j-1}^n - T_{i,j}^n}{R_{cond\_cyl\_r} + R_{conv\_cyl\_r}} + \frac{T_{i,j+1}^n - T_{i,j}^n}{R_{cond\_cyl\_r} + R_{cond\_ins\_r}} + \frac{T_{i-1,j}^n - T_{i,j}^n}{R_{cond\_cyl\_z}} + \frac{T_{i+1,j}^n - T_{i,j}^n}{R_{cond\_cyl\_z}} \tag{27}$$

Heat equation applied to the insulation is given by,

$$\rho_{ins} c_{p\,ins} \Delta V_{ins} \frac{T_i^{n+1} - T_i^n}{\Delta\tau} = \frac{T_{i,j-1}^n - T_{i,j}^n}{R_{cond\_cyl\_r} + R_{cond\_ins\_r}} + \frac{T_\infty^n - T_{i,j}^n}{R_{cond\_ins\_r}} + \frac{T_{i-1,j}^n - T_{i,j}^n}{R_{cond\_ins\_z}} + \frac{T_{i+1,j}^n - T_{i,j}^n}{R_{cond\_ins\_z}} + \frac{(T_\infty^n)^4 - (T_{i,j}^n)^4}{R_{rad\_ins\_r}} \tag{28}$$

The cavity receiver is discretized into cylindrical control volumes with cylinder length Δz. The control volume length changed at disc and after disc sections to be Δz_2 and Δz_3respectively, where Δz_2 represents disc thickness. Heat equation applied to the cavity disc is given by,

$$\rho_{disc} c_{p_{disc}} \Delta V_{disc} \frac{T_i^{n+1} - T_i^n}{\Delta\tau} = Q_{\mathrm{int}}(\pi r_1^2) + \frac{T_{i,j+1}^n - T_{i,j}^n}{R_{cond\_disc\_r} + R_{conv\_disc\_r}} + \frac{T_{i-1,j}^n - T_{i,j}^n}{R_{cond\_cav\_z}} + \frac{T_{i+1,j}^n - T_{i,j}^n}{R_{cond\_disc\_z} + R_{conv\_disc\_z}} \tag{29}$$

Heat transfer equation for nozzle plenum section,

$$\rho_{fl} c_{p\,fl} \Delta V_{out} \left(\frac{T_i^{n+1} - T_i^n}{\Delta\tau} \right) = \frac{T_{i-1,j}^n - T_{i,j}^n}{R_{cond\_disc\_z} + R_{conv\_disc\_z}} + \frac{T_{i,j+1}^n - T_{i,j}^n}{R_{cond\_cyl\_r} + R_{conv\_cyl\_r}} + \dot{m} c_{p\,fl} (T_{i-1,j+1}^n - T_{i,j}^n) \tag{30}$$

For solid parts in the cavity receiver design such as the cavity and outer cylinder which are designed from tungsten and steel respectively, the change in the thermal properties can be neglected. On the other hand, for the working fluid (hydrogen) and the outer insulation (fiberform) the change in thermal properties with temperature are significant. Variable properties are thermal conductivity *k*, specific heat capacity at constant pressure c_p and the dynamic viscosity μ. Change in thermal properties with temperature is considered in the computer code.

Change in thermal properties of the propellant (hydrogen) as a function of temperature can be given by,

$$k_{hyd} = 0.00517975\ \ 922 + 6.72778\ \times 10^{-4}\,\mathrm{T} - 3.0388973\ \times 10^{-7}\,\mathrm{T}^2 + 6.58874687\ \times 10^{-11}\,\mathrm{T}^3 \tag{31}$$

$$c_{p\,hyd} = 10808.501 + 21.5799904\,\mathrm{T} - 0.04447203\ 18\mathrm{T}^2 + 3.85401176 \times 10^{-5}\,\mathrm{T}^3 - 1.14979447 \times 10^{-8}\,\mathrm{T}^4 \tag{32}$$

$$\mu_{hyd} = 2.14524642\ \times 10^{-6} + 2.54245 \times 10^{-8}\,\mathrm{T} - 1.0235587\ \times 10^{-11}\,\mathrm{T}^2 + 2.80895021\ \times 10^{-15}\,\mathrm{T}^3 \tag{33}$$

Change in specific heat and thermal conductivity of the insulation material (fiberform) can be determined by,

$$c_{p\,ins} = 756.96 + 0.95769\mathrm{T} - 1.5402\times10^{-3}\mathrm{T}^2 + 1.3509\times10^{-6}\mathrm{T}^3 - 5.2031\times10^{-10}\mathrm{T}^4 + 7.1506\times10^{-14}\mathrm{T}^5 \tag{34}$$

$$k_{ins} = 0.19999\ \ -1.3853\ \times 10^{-4}\,\mathrm{T} + 7.6844\ \times 10^{-8}\,\mathrm{T}^2 - 2.4532\ \times 10^{-11}\,\mathrm{T}^3 \tag{35}$$

After formulating the resistance network and writing the discretized form of the equations, a computational code is developed to solve system of equations. The equations are written in backward difference and result in a system of equations of the form,

$$[A]_{i_{\max} j_{\max} \times i_{\max} j_{\max}} T_{i,j}^{n+1} = [B]_{i_{\max} j_{\max}} T_{i,j}^{n} + [C]_{i_{\max} j_{\max}} \quad (36)$$

Matrix [*A*] includes the coefficients of temperature at each node for the existing time step. Matrix [*B*] includes coefficients for the previous time step, and matrix [*C*] includes the boundary conditions. Solving this system gives the temperatures for each node at any required time level. Matrix [*A*] is inverted at each time level to obtain new temperature values with respect to previous ones. To formulate matrices [*A*], [*B*] and [*C*], the receiver section is discretized into 300 longitudinal sections, each section includes four layers in the radial direction. Each block in matrix [*A*] represents a complete axial section with its four layers.

E. Radiation Analysis

The amount of energy lost by radiation represents a significant ratio of the input power that can affect the whole system performance. Radiation losses can be divided into two types. First the thermal radiation losses which arise from the temperature difference between cavity receiver and ambient conditions given by,

$$\begin{aligned} Q_{rad} &= \sigma \varepsilon_{cav} F_{ca} A_{wall} (T_{cav}^4 - T_{amb}^4) \\ &+ \sigma \varepsilon_{cav} F_{da} A_{disc} (T_{disc}^4 - T_{amb}^4 \end{aligned} \quad (37)$$

Here ε_{cav} is the cavity material emissivity; A_{rad} is the area of the radiating surface. T_{cav} is the cavity temperature, T_{disc} is the disc temperature and T_{amb} is the ambient temperature. F_{ca} is the view factor between cavity wall and cavity aperture and F_{da} is the view factor between cavity disc and cavity aperture. View factors can be determined from equations (38) and (39).

$$F_{ca} = \frac{\sqrt{4\left(\frac{d_{cav}}{L_{cav}}\right)^2 + 1} - 1}{4\left(\frac{d_{cav}}{L_{cav}}\right)} \quad (38)$$

$$F_{da} = 1 - \frac{\sqrt{4\left(\frac{d_{cav}}{L_{cav}}\right)^2 + 1} - 1}{2\left(\frac{d_{cav}}{L_{cav}}\right)^2} \quad (39)$$

The other source of radiation loss is due to the reflected rays from the cavity surface which can be represented by,

$$Q_{ref} = Q_{\text{int}} (1 - \alpha_{eff}) \quad (40)$$

Here Q_{ref} is the radiation loss due to reflection, α_{eff} is the effective absorptance of the receiver and Q_{int} is the total intercepted power by the receiver from the concentrator. The effective absorptance of the cavity receiver is given by [9],

$$\alpha_{eff} = \frac{\alpha_{cav}}{\alpha_{cav} + (1 - \alpha_{cav})(A_{ap} / A_{cav})} \quad (41)$$

The cavity material absorptance is α_{cav}, A_{ap} is the cavity aperture area and A_{cav} is the inner surface area of the cavity. Adding a glass cover to the cavity aperture is a good solution to reduce the energy lost by radiation. Although the glass cover will decrease the amount of energy intercepted by the cavity receiver but it isolates the inner cavity surface from the ambient which helps in decreasing the thermal radiation losses. The reflected radiation value will change according to the transmittance of the glass cover. Equation 39 is modified in case of adding a glass cover to be,

$$Q_{ref} = Q_{\text{int}} (1 - \tau_g \alpha_{eff}) \quad (42)$$

Transmittance of glass cover material is τ_g. In case of adding a glass cover the effective absorptivity for the cavity can be determined using equation 3.52, where the term τ_d represents the glass cover transmittance to diffuse radiation which can be approximated to be 0.82. The effective absorptivity is given by [9],

$$\alpha_{eff} = \frac{\alpha_{cav}}{\alpha_{cav} + (1 - \alpha_{cav})\tau_d (A_{ap} / A_{cav})} \quad (43)$$

F. Initial and Boundary Conditions

Initial conditions vary from one case to another. For the test case the cavity receiver is assumed to be tested in a vacuum chamber at temperature 298°K. Therefore the initial temperature for all cavity receiver parts is 298°K. In other analyses such as hot start case initial temperatures changes. In the hot start case the cavity initial temperature increases (1000°K and 2000°K).The boundary conditions are shown in Fig. 6 and can be described as follows:

- **Radiation boundaries:** Radiation boundaries exist in the internal cavity surface and the outer insulation boundary.
- **Convection boundaries:** Convection boundaries represent the internal convection from the cavity and cylinder to the fluid bounded by them. Boundary (a) shown in Fig. 6 represents the convection from the cavity outer surface to the fluid. Boundary (b) represents the internal convection from the cavity disc to the fluid. Boundary (c) represents the internal convection from the outer cylinder to the fluid.
- **Fluid inlets:** The fluid inlet conditions are that for stored hydrogen inside the tank. Hydrogen is assumed to be stored at standard conditions, then the inlet fluid temperature is 298°K and pressure is 1 bar.

- **Fluid outlet:** The outlet fluid temperatures are extrapolated from the inside domain.
- **Intercepted solar power:** The value of intercepted solar power is computed from the concentrator dish analysis which was discussed in chapter two. The intercepted power from the dish is assumed to be equally distributed on the inner cavity surface.

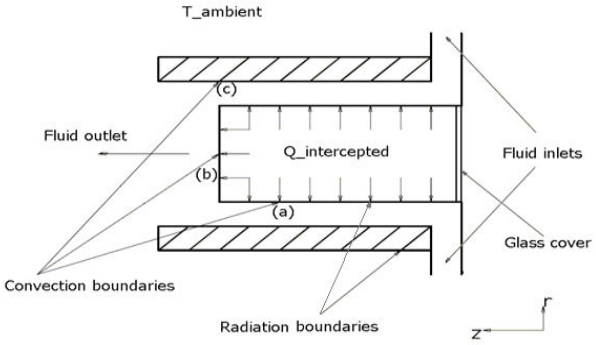

Fig. 6 Cavity receiver boundary conditions

V. Applications

A. Propulsion Application

In this application, the addition of a nozzle to produce thrust is considered as shown in Fig. 1. After the total temperature of the working fluid through the cavity receiver is raised, the fluid is expanded through the nozzle in order to convert the energy to thrust. Thrust force can be controlled by many factors such as mass flow rate, fluid exit velocity, exit pressure and exit to throat area ratio. The nozzle is responsible for raising the fluid exit velocity which results in increasing the output thrust force from the engine. Quasi one dimensional solution for the fluid flow inside nozzle is performed [14]. After determining the throat area required for the fluid to be chocked, the flow properties can be calculated in the nozzle using the area relation and the isentropic flow equations. After that the thrust and specific impulse can be computed.

The output thrust force from nozzle is given by the relation,

$$F_{th} = \dot{m} V_{exit} + (P_{exit} - P_{\infty}) A_{exit} \quad (44)$$

Factors affecting thrust force are propellant mass flow rate, exit propellant velocity V_{exit}, exit nozzle area A_{exit} and the pressure difference between nozzle exit and ambient.

The value of specific impulse can be related to thrust force as given by,

$$I_{sp} = \frac{F_{th}}{\dot{m} g_o} \quad (45)$$

The thruster performance is represented by the specific impulse. Higher value of specific impulse reflects the capability of the thruster to produce higher thrust with the same propellant consumption. Ideal specific impulse relation with the propellant temperature is given by,

$$I_{sp} = \frac{1}{g}\sqrt{\left(\frac{2\gamma}{\gamma-1}\right)\left(\frac{gRT_{fl}}{M_{fl}}\right)\left(1-\frac{p_c}{p_e}\right)^{\frac{\gamma-1}{\gamma}}} \quad (46)$$

where R is the gas constant, T_{fl} is the propellant temperature at cavity receiver, M_{fl} is the molecular weight, p_c is the cavity receiver pressure and p_e is the external pressure.

A comparison between three different propellants which are air, helium and hydrogen is considered to define the most adequate propellant that improves the thruster performance.

B. Electricity Generation Application

The main target of this application is to investigate the modifications for converting the solar thermal engine to a power generation engine for electricity generation as shown in Fig. 2.Main subsystems developed in the design (concentrator dish and cavity receiver) are used as is, while others are redesigned. The nozzle is replaced by a compressor and turbine. The fundamental thermodynamic cycle used with solar conversion systems is the Brayton cycle. Brayton cycle is implemented using a compressor for the 1st process, solar radiation heating for the 2nd process, a turbine for the 3rd process and heat rejection to the atmosphere in the 4th process. To analyze the cycle all the states need to be evaluated. The first law of thermodynamics determines energy transfer. Flow states through the compressor and the turbine are assumed to be isentropic flow [13].

In this analysis the following assumptions are made:

- The working fluid is air and treated as an ideal gas throughout the cycle.
- Air heating process is modeled as a constant-pressure heat addition process.
- Exhaust air is modeled as a constant-pressure heat rejection process.
- Mass flow rate is fixed throughout the entire cycle.
- The system operates at steady state.
- There are negligible kinetic and potential energy changes.

The thermodynamic cycle thermal efficiency can be computed in terms of compression ratio as shown in equation 46.

$$\eta_{th} = 1 - \frac{1}{(r_c)^{(\gamma-1)/\gamma}} \quad (47)$$

where, r_c represents the ratio between pressures at exit and inlet compressor states.

VI. Results

A. Concentrator Dish Results

Table I represents a comparison between output results from the performed computer code and the published results [4].

TABLE I
OUTPUT CONCENTRATOR POWER VALIDATION WITH PUBLISHED RESULTS

Concentrator Type	Output power (Published results)	Output power (Numerical model results)	Variation Percentage
JPL	(62 kW), At DNI 800 W/m^2	(61.12 kW)	1.4 %
Vanguard I	(76.4 kW) At DNI 1000 W/m^2	(73.6 kW)	3.7 %
Acurex	(162 kW) At DNI 1000 W/m^2	(157.79 kW)	2.6 %
Schlaich, Bergermann und Partner	(36.2 kW) At DNI 1000 W/m^2	(36.53 kW)	0.9 %
DOE Faceted Stretched membrane	(70 kW) At DNI 1000 W/m^2	(70.16 kW)	0.2 %

The design based on 1000 W/m^2 beam normal insolation. In space the value of beam normal insolation is higher than the selected value which results in decreasing the concentrator dish size. Through the parametric study the design parameters of the concentrator dish will be selected.

Fig. 7 represents the decay in the intercept factor for each differential ring (flux capture fraction). Results show that intercepted power from a differential ring near the concentrator vertex is higher than that for another differential ring near the concentrator rim.

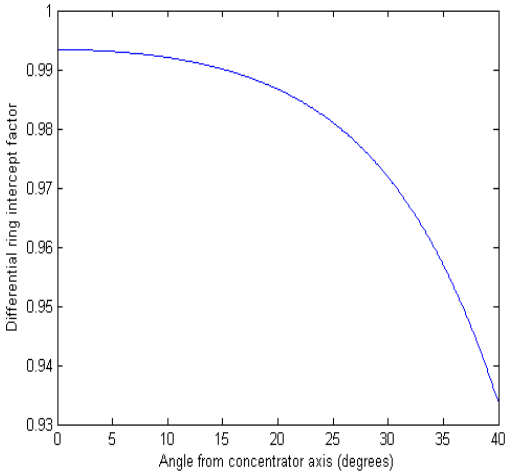

Fig. 7 Differential rings intercept factor from concentrator axis to the rim

Fig. 8 represents the effect of concentrator diameter on the optical efficiency for a fixed receiver aperture equal to 20 cm.

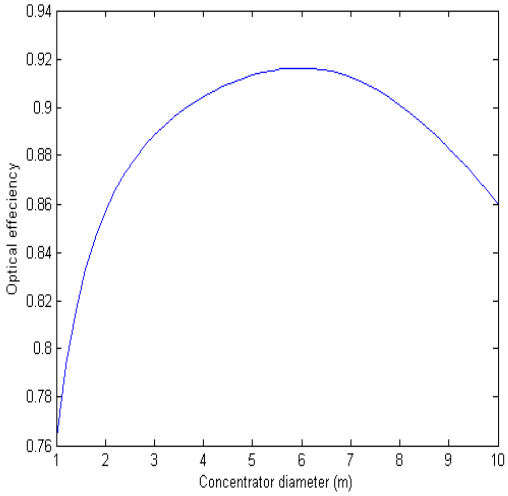

Fig. 8 Concentrator diameter effect on optical efficiency

The effect of the rim angle on the optical efficiency is shown in Fig. 9.The optical efficiency reaches its maximum at 45 degrees as shown in figure. The selected concentrator rim angle in our design is 40 degrees, since most designers use a rim angle close to the optimum (±5^o).

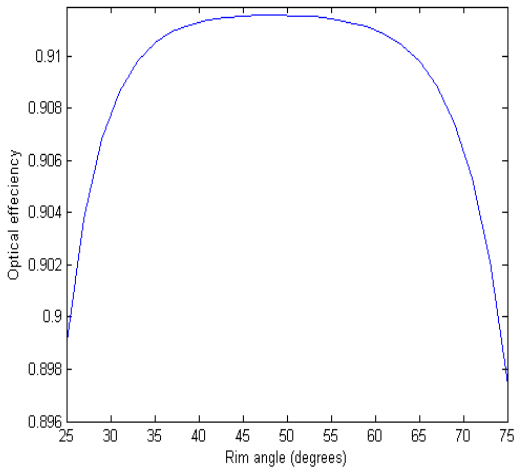

Fig. 9 Rim angle effect on optical efficiency

Concentrator diameter must be identified as there is a coupled effect between both concentrator and receiver diameters and the intercepted power. If the required input power to the receiver is 10 kW, then the required concentrator is 4 meters in diameter and the most adequate receiver aperture diameter is about 10 cm as seen from Fig. 10.

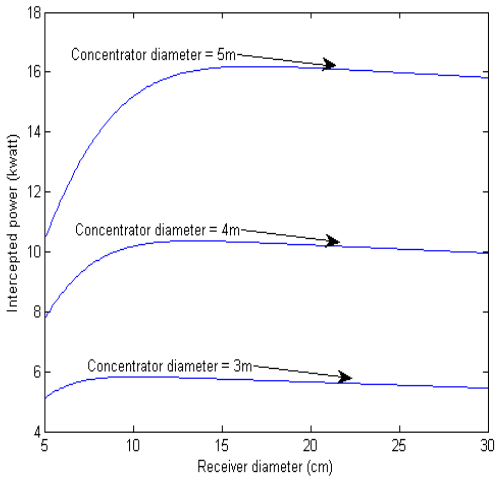

Fig. 10 Receiver diameter effect on intercepted power at various concentrator diameters

B. Cavity Receiver Results

In the following results, the code is applied on an initial design which has the following specifications. Cavity receiver length is 41.4 cm and outer diameter is 26.2 cm. Inner cavity length is 38 cm and about 6.7 cm in diameter. Outer cylinder diameter is 9.2 cm. All solid layers thicknesses are set to 1 mm as an initial guess and the insulation thickness is 8.38 cm. Input solar power from the concentrator equals to 10 kW. This model is assumed to be tested in a thermal vacuum chamber at 298^{o}K using initial and boundary conditions discussed before. Fluid mass flow rate for testing case is 0.25 g/sec. The implicit scheme can use a $\Delta\tau$=10 seconds, without having any stability problems. Most of the initial cavity receiver design parameters are given NASA MSFC [1], and missing parameters for the thruster are assumed [2], [6]. This design is considered to be a starting point which will be enhanced through the parametric study to enhance performance.

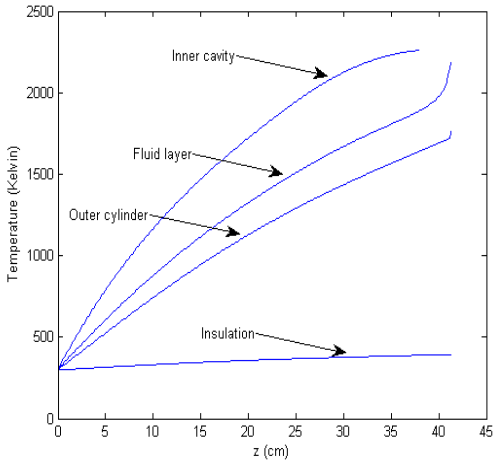

Fig. 11 Different layers transient results after 30 minutes of operation

Fig. 11 shows the temperature along the cavity receiver in the four radial layers after 30 minutes of operation. The longitudinal axis represents the position along the receiver length and each curve represents the temperature distribution in each layer.

The fluid layer is the most important for identifying the receiver performance. Fig. 12 shows the transient results for the fluid layer at different periods from operating the cavity receiver. The sudden change in the temperatures at the last cavity section is due to the high value of convection heat transfer from the cavity disc to the fluid at the plenum.

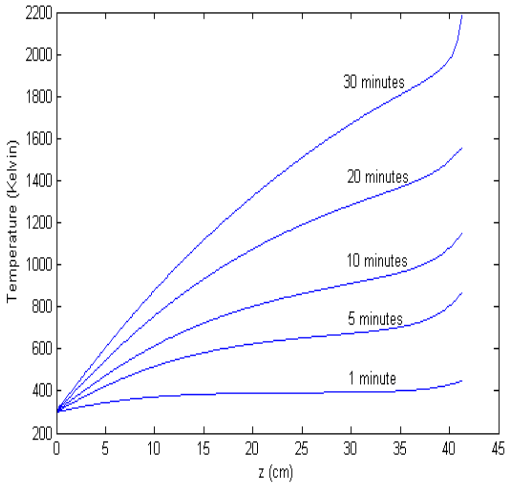

Fig. 12 Fluid layer temperatures at different time steps

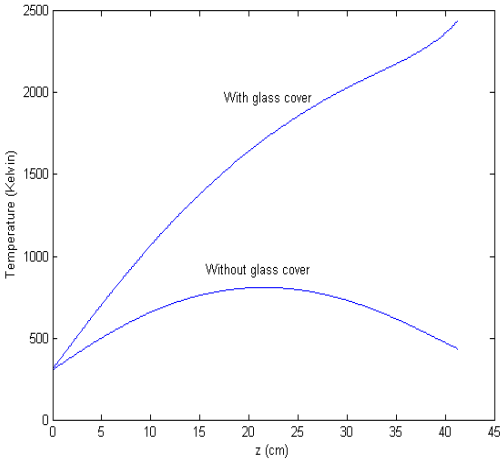

Fig. 13 Fluid layer steady state temperatures with and without glass cover

The effect of cavity radiation loss on the fluid layer temperatures is shown in Fig. 13. It can be observed that the cavity radiation loss results in observable decrease in the working fluid temperature along the cavity receiver. Cavity radiation loss due to emission decreases the plenum temperature to be less than 500^{o}K. It is seen that using a glass

cover reduces the losses significantly and must be incorporated in the design.

One of the important drawbacks to achieve higher temperatures in the proposed design is the slow response of the system. That is because the system must work about 30 minutes in order to reach a fluid temperature near to 2000°K. This case is not applicable in space since the fluid storage is limited. This slow response will result in a significant amount of propellant loss. Alternatively, a hot start can be performed in which the fluid flows after the receiver is pre-heated by the solar radiation.

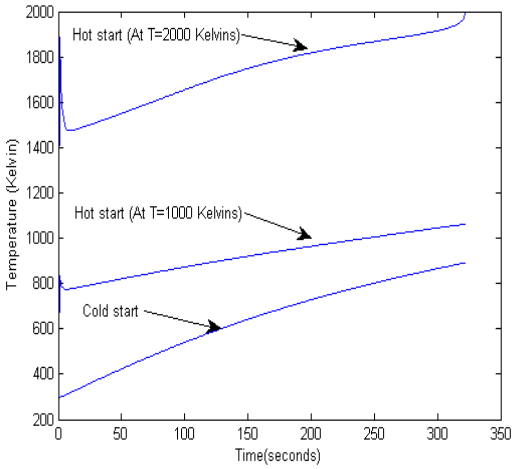

Fig. 14 Plenum temperature at hot and cold start

In the sensitivity study different design parameters are concerned to determine its effect on the cavity receiver performance which enables in the enhancement of the design.

Mass flow rate is an input to our code, as it can be controlled from outside the receiver. Fig. 15 shows the inverse relation between mass flow rate and the fluid temperature.

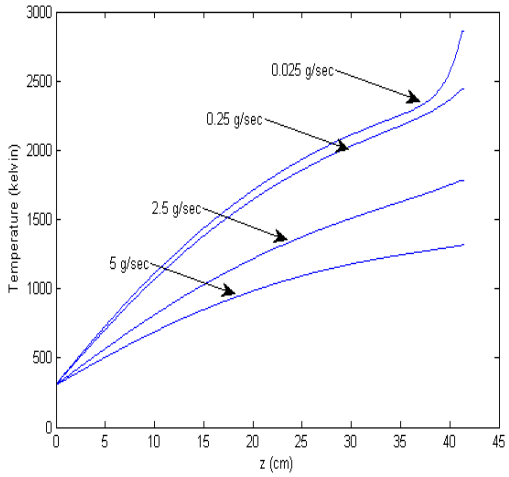

Fig. 15 Mass flow rate effect on fluid temperature

Increase of mass flow rate decreases the fluid temperature at every point in the fluid layer. This is expected since the heat flux is fixed. The horizontal axis of the figure represents the position along the cavity receiver length. The vertical axis represents the temperatures in Kelvin.

The effect of the inner cavity length and diameter is considered. On the contrary to the receiver outer cylinder length, the cavity receiver sensitivity study shows the high dependence of the cavity receiver length on the receiver outlet temperature and receiver performance. Fig. 16 shows that increasing the inner cavity length from 20 cm to 40 cm increase the plenum temperature about 2 times.

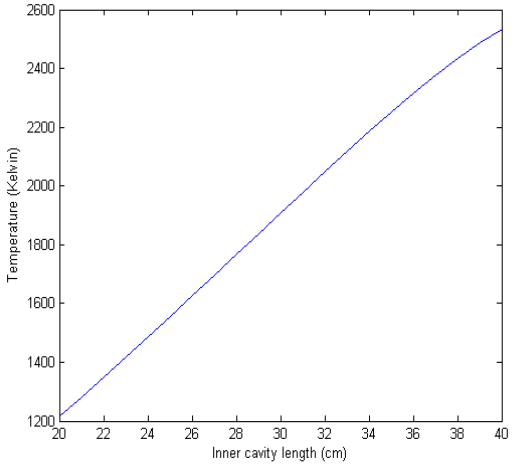

Fig. 16 Inner cavity length effect on outlet receiver temperature

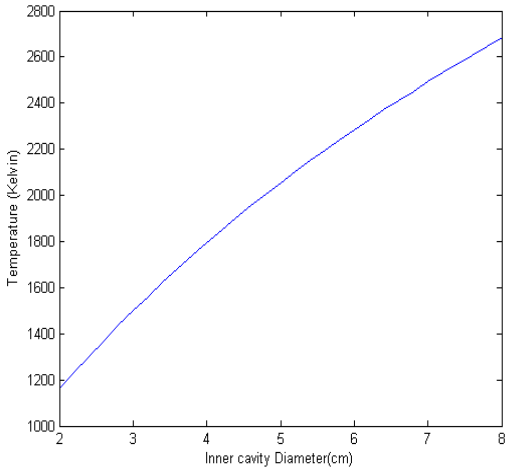

Fig. 17 Inner cavity diameter effect on outlet receiver temperature

The effect of insulation thickness on outlet receiver temperature is shown in Fig. 18.Thick insulation helps in decreasing energy lost from cavity wall to ambient. Fig.18 shows that increasing the insulation thickness from 1 cm to 10 cm causes a significant change in the steady state temperature at the receiver outlet. The effect of the insulation layer thickness on performance starts to decrease after 10 cm thickness; therefore an adequate selection of the insulation

layer thickness will be 10 cm.

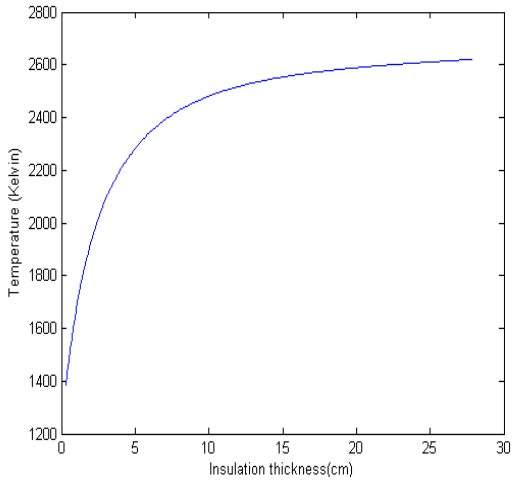

Fig. 18 Insulation thickness effect on outlet receiver temperature

The influence of changing thicknesses of cavity receiver is discussed. All thicknesses vary from 1 mm to 3 mm as shown in Fig. 19. Results reflect that the effect of increasing both inner cavity and outer cylinder thicknesses decrease achieved temperature at plenum. On the other hand, the increase in both disc thickness and fluid layer thickness cause the plenum temperature to increase. Therefore, it can be concluded that decreasing the cavity and cylinder thicknesses improves the performance. Also increasing the disc thickness improves the performance. The cylinder and cavity thicknesses will be set to 1 mm and the disc thickness will be set to 3 mm.

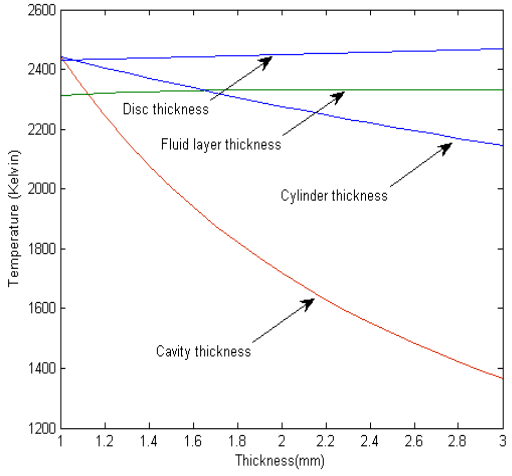

Fig. 19 Different layers thicknesses effect on outlet receiver temperature

The cavity receiver initial and improved design parameters are listed in Table II.

TABLE II
CAVITY RECEIVER INITIAL AND IMPROVED DESIGN PARAMETERS

Design parameter	Initial design	Improved design
Cavity length	41.4 cm	50 cm
Inner cavity length	38 cm	47 cm
Cylinder diameter	9.2 cm	10 cm
Cavity diameter	6.7 cm	8 cm
Outer insulation diameter	26.2 cm	30.2 cm
Cavity thickness	1 mm	1 mm
Cylinder thickness	1 mm	1 mm
Disc thickness	1 mm	3 mm
Fluid layer thickness	2.26 cm	2 cm
Insulation thickness	8.38 cm	10 cm
Input solar power	10 kW	10 kW
Propellant type	*Hydrogen*	*Hydrogen*
Mass flow rate	0.25 g/sec	0.1 g/sec

Fig. 20 represents the transient results of the fluid temperatures along the receiver. The fluid temperature at plenum reaches 3071°K after 30 minutes of operation. Comparing these results with that obtained in the initial design, one can observe the improvement in the cavity receiver performance. The plenum temperature increases in the improved design by 913°K after the same period of operation under cold start operation conditions.

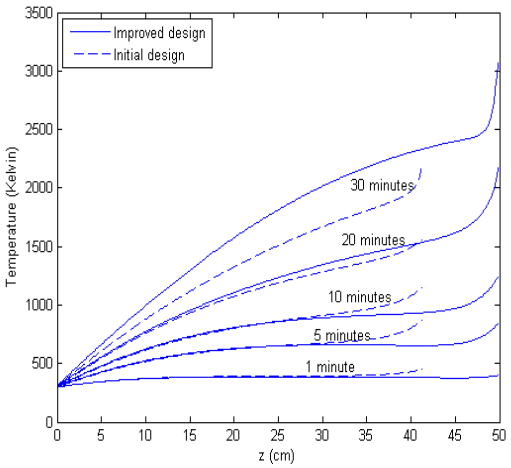

Fig. 20 Improved design comparison with initial design

C. Propulsion Application Results

The solar thruster or the solar thermal rocket is characterized by its high specific impulse on the order of 850 to 1100 seconds [3]. The reason of high specific impulse is that it is inversely proportional with the propellant molecular weight [1].

Fluid properties are solved along the nozzle (10 cm length) for different working fluid types. The working fluid velocity distribution is shown in Fig. 21.

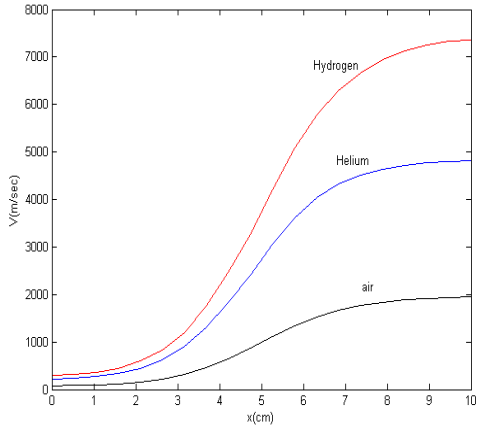

Fig. 21 Velocity distribution for different fluids along nozzle

A comparison for different gases is shown in Table III. The comparison shows the effect of the gas on output thrust and specific impulse which act as the main parameters to judge the nozzle performance.

TABLE III
THRUST AND SPECIFIC IMPULSE FOR DIFFERENT PROPELLANTS

Working fluid	Thrust (Newton)	Specific Impulse (sec)
Hydrogen	1.94	784.62
He	1.24	502.75
Air	0.51	207.78

Propellant mass flow rate is an effective parameter in our sensitivity study. Increasing the propellant flow rate during the complete mission time wastes fuel, therefore it must be pulsed to the engine in a controlled manner to achieve the required thrust.

Fig. 22 represents the effect of mass flow rate on the outlet receiver temperature (inlet nozzle temperature).

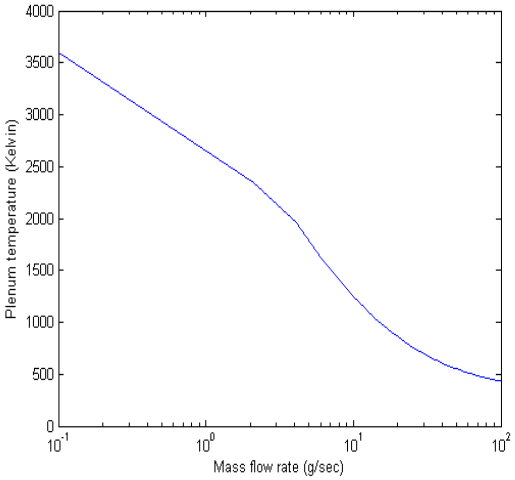

Fig. 22 Mass flow rate effect on inlet nozzle temperature

Results show that the increase in mass flow rate causes a significant drop in the inlet nozzle temperature.

Fig. 23 shows that the increase in mass flow rate causes a valuable increase in the nozzle thrust. Increase in mass flow rate causes decrease in the specific impulse as seen in Fig.24. The results show that at mass flow rate of 0.1 g/sec the cavity receiver outlet temperature is 3603^{o}K. The values of output thrust and specific impulse are 0.97 Newton and 991.69 seconds, respectively.

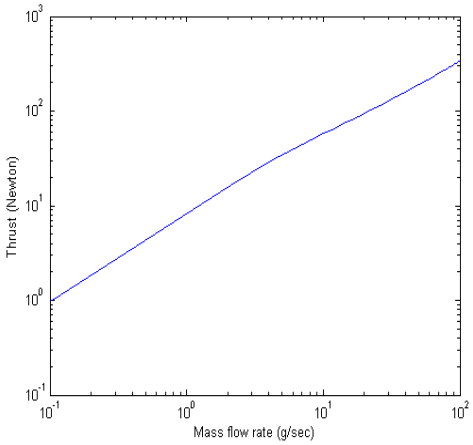

Fig. 23 Mass flow rate effect on output thrust force

These results are more suitable for systems that require high values of specific impulse. But, in some cases during a mission the value of thrust is the most important parameter. Higher values of thrust can be achieved from the thruster model by increasing the values of mass flow rate. The thrust value is 338.16 Newtons at mass flow rate 100 g/sec. This increase in thrust will be accompanied by a decrease in the specific impulse value to be 344.36 seconds as seen in Fig. 24.

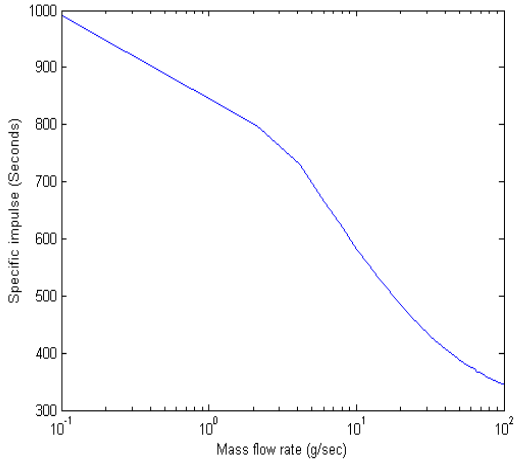

Fig. 24 Mass flow rate effect on specific impulse

Although working at high values of mass flow rate achieves

higher thrust but the solar thruster performance drops below that of the chemical thrusters which achieves 450 seconds as an average value of specific impulse. The performance of the designed solar thruster reaches that of chemical thrusters at 26.1 g/sec mass flow rate and the thrust value is 115.6 Newtons, therefore it is not preferred to exceed this value of mass flow rate during the thruster operation.

The most important advantage in solar thermal thrusters is the high specific impulse values that can be achieved with a moderate thrust values. Therefore, the suggested value of mass flow rate is 1 g/sec. At this value the plenum temperature is 2791.3^{o}K. The thrust and specific impulse values are 8.56 Newtons and 872.87 seconds, respectively.

D. Power Generation Application

The selected concentrator diameter is 4 meters to develop 10 kW (this result based on concentrator analysis). Receiver design parameters are selected as the improved model, the receiver length is 50 cm and 10 cm in diameter. The working fluid is selected to be atmospheric air at inlet temperature 298^{o}K and pressure is 1 atm [7]. All results will be at an initial value of mass flow rate which is 10 g/sec.

TABLE IV
OUTPUT RESULTS AND THERMAL EFFICIENCY

	State 1	State2	State 3	State 4
Temperature (K)	298	575.3	1571.9	814.1
Pressure (pa)	1.01325 x10^5	10.1325 x10^5	10.1325x 10^5	1.01325x 10^5
Output work from the turbine		760.4 (kJ/kg)		
Work required by the compressor		278.3 (kJ/kg)		
Net power		4.82 (kW)		
Thermal efficiency		48.2 %		

As seen from Fig. 25 that a higher compression ratio improves the engine thermal efficiency. Compression ratio rising from 5 to 25 increases the thermal efficiency nearly 20% or more which is a significant result.

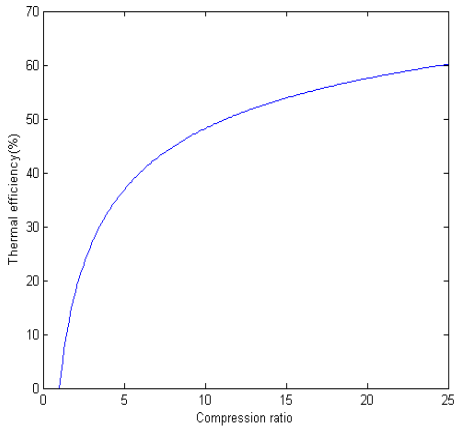

Fig. 25 Thermal efficiency variation with compression ratio

The selected compression ratio is 10 because this can be achieved by a moderate compressor. Increasing this value requires a costly compressor which is not preferred for the economical efficiency of the power generation engine to be used as a home electricity generation device.

The limitation on increasing mass flow rate which was mentioned in the space application was due to the limited amount of hydrogen inside the tank. This limitation is not taken into consideration in the current power generation device as the working fluid is atmospheric air, therefore increasing mass flow rate to higher values will be available if it improves the system performance. The problem is the coupled effect between mass flow rate and turbine inlet temperature (TIT), which causes a decrease in TIT with increasing mass flow rate. Fig. 26 shows that the increase in mass flow rate accompanied by decrease in the TIT.

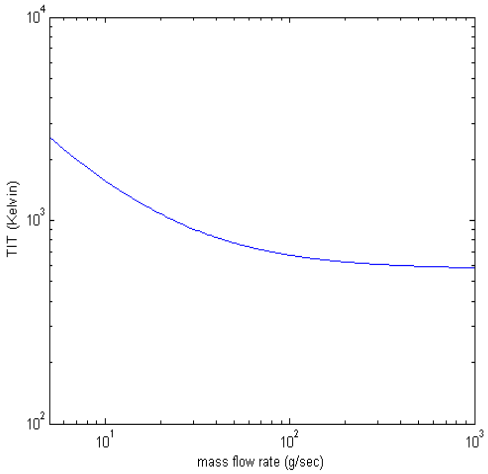

Fig. 26 Mass flow rate variation with turbine inlet temperature

Fig. 27 represents the net output work versus mass flow rate at different compression ratios.

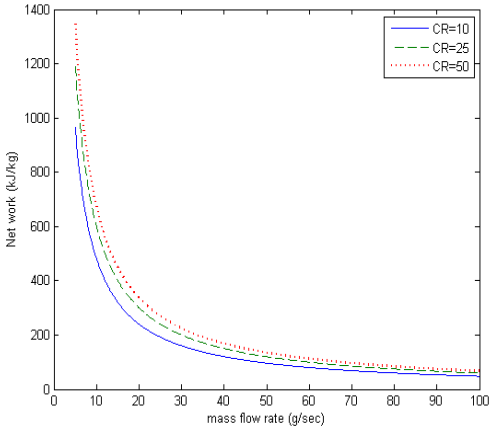

Fig. 27 Net output work versus mass flow rate at different compression ratios

The results show a decay of the net output work with increasing the mass flow rate of the working fluid. The value of compression ratio has a significant effect on the performance of the engine, especially at low values of mass flow rate. At higher values of mass flow rate the net output work decreases and also the effect of compression ratio.

VII. Conclusions

For both space and electric power generation, a 10 kW system is targeted. For this the concentrator (a parabolic dish) is used with a diameter of 4 meters and 10 cm cavity receiver diameter is selected. The focal length of this system is at 2.75 meters and the optimum rim angle is 45^o.

There is a limitation on increasing the concentrator diameter with respect to the receiver due to the optical losses which decreases the system efficiency.

The cavity receiver is modeled using an unsteady lumped capacity resistance model. The results show:

- Two sources of radiation losses affect the outlet propellant temperature from the cavity receiver which are emission and reflection losses. The most critical are the emission losses that arise from temperature difference between the inner cavity and ambient conditions. A glass cover at the cavity mouth decreases both emission and reflection losses from the cavity interior surface to the ambient.
- Working at cold start operating conditions was found to be not efficient for the thruster operation due to the limited amount of propellant inside the tank. Starting the fluid flow at hot start condition 2000^{o}K improves the thruster performance.
- The explicit solution of the model is not possible since stability requirements require a very small time step. An implicit technique is used to avoid high computational cost. Higher order terms such as radiation terms were treated using iteratively implicit technique.
- The most effective parameter in the sensitivity study is the mass flow rate. Results show that working at low values of mass flow rate increases the plenum temperature.

The nozzle is attached to the concentrator/cavity receiver for the STP model. The nozzle is modeled as a quasi-one dimensional flow assuming shockless isentropic flow.

A comparison between different propellant types was performed between air, helium and hydrogen. Hydrogen proved to be the most preferred propellant.

Parametric study shows that mass flow rate is the key to control the required thrust and specific impulse of the thruster. Increasing the mass flow rate from 1 g/sec to 2 g/sec will increase the thrust from 8.56 Newtons to 15.79 Newtons but on the other hand a drop in the specific impulse value from 872.87 seconds to 804.98 seconds will occur which means that the operator consumes more propellant from the tank.

The concentrator/cavity receiver are also attached to a compressor/turbine power cycle. Here a cycle based on the Brayton cycle is suggested where the heat source is the solar input flux. The working fluid is the atmospheric air. The analysis suggests that using a moderate compression ratio of 10 results in thermal efficiency of 48.2%.

Increasing the compression ratio increases the thermal efficiency however the size of the compressor (and cost) would be too prohibitive (e.g. for a compression ratio of 25, the thermal efficiency is 60.14% and cost will be higher due to the required compressor is more expensive).

The parametric study suggests that the compression ratio and mass flow rate are the most effective parameters on the efficiency. The coupled effect of mass flow rate on TIT is considered. Increasing the mass flow rate causes decrease in the TIT which decrease the thermal efficiency. It was decided to work at low values of mass flow rate. The selected value of mass flow rate is 5 g/sec.

As a whole conclusion, a power generation engine using a compressor with pressure ratio 10 and operated at air mass flow rate 5 g/sec can achieve net output power 4.82 kW which is sufficient to be used as a home electricity generation device.

Acknowledgment

I have greatly appreciated to my supervisor Prof. Ibrahim M. Shabaka for his technical advices. I would also like to give special thanks to my supervisor Dr. Basman M. Elhadidi for his help and support. Finally, I like to thank my institute NARSS.

References

[1] H. W. Coleman and R. A.Alexander, "Thermal Characterization of a Direct Gain Solar Thermal Engine", NASA Marshall Space Flight Center, AIAA Journal of Spacecraft and Rockets, October 1999.
[2] M. Shimizu, et al., "Single Crystal Mo Solar Thermal Thruster for Microsatellites", 49thInternational Astronautical Federation Published by Elsevier Science , Vol. 44, Nos. 7-12, pp. 345-352, 1999.
[3] T.Nakamura, et al., "Solar Thermal Propulsion for Small Spacecraft", 41st AIAA/ASME/SAE/ASEE Joint Propulsion Conference, Tucson AZ, July 10-13, 2005.
[4] R. B. Diver and W. B. Stine, "A Compendium of Dish/Stirling Technology", Sandia National Laboratories Technical Report, SAND93-7026 UC-236, Livermore, California, USA, January, 1994.
[5] M. De Carli, et al., "A Computational Capacity Resistance Model (CaRM) for vertical ground-coupled heat exchangers", International Journal of Renewable Energy, 35 (2010) 1537–1550, 2010.
[6] G. Colonna, et al., "A Model for Ammonia Solar Thermal Thruster", 38th AIAA Thermophysics Conference, Toronto, Ontario Canada, June 6-9, 2005.
[7] K. Bammert, A. Hegazy and P. Seifert, "Determination of Radiation Distribution in Solar Heated Receivers with Parabolic Dish Collectors",5th International Conference for Mechanical Power Engineering, Ain Shams University, Cairo, Egypt, October, 1984.
[8] C. C. Newton and A. Krothapalli, "A Concentrated Solar Thermal Energy System", Florida State University, 2007.
[9] P. R. Fraser, A. K. Sanford, "Stirling Dish System Performance Prediction Model", University of Wisconsin Madison, 2008.
[10] Y. A. Abdel-Hadi, A. Ding, H. J. Eichler and E.Sedlmayr, "Development of optical concentrator systems for directly solar pumped laser systems", Technical University of Berlin, Institute of Optics, Berlin, 2008.
[11] S. Kalogirou, "Solar Energy Engineering Processes and Systems", 1st Edition. California, USA, 2009.
[12] J. P. Holman, "Heat Transfer", 8th Edition.
[13] V. Wylen, et al, "Fundamentals of Thermodynamics", 5th Edition.
[14] J. D. Anderson, "Modern Compressible Flow", 2nd Edition.